Supplementary Information

Lithium magnesium alloys: a framework for investigating lithium alloy anodes for solid state batteries.

Jack Aspinall[a,b], Krishnakanth Sada[a,b], Hua Guo[a,b], Sudarshan Narayanan[a,c], Yvonne Chart[a,b], Ben Jagger[a], Emily Milan[a], David Armstrong[a,b], and Mauro Pasta[a,b,*]

[a]Department of Materials, University of Oxford, Parks Road, Oxford OX1 3PH, United Kingdom
[b]The Faraday Institution, Harwell Campus, Quad One, Becquerel Avenue, Didcot OX11 0RA, United Kingdom
[c]Department of Sustainable Energy Technology, Indian Institute of Technology, Kanpur, 208016, India

[*]Corresponding author: mauro.pasta@materials.ox.ac.uk

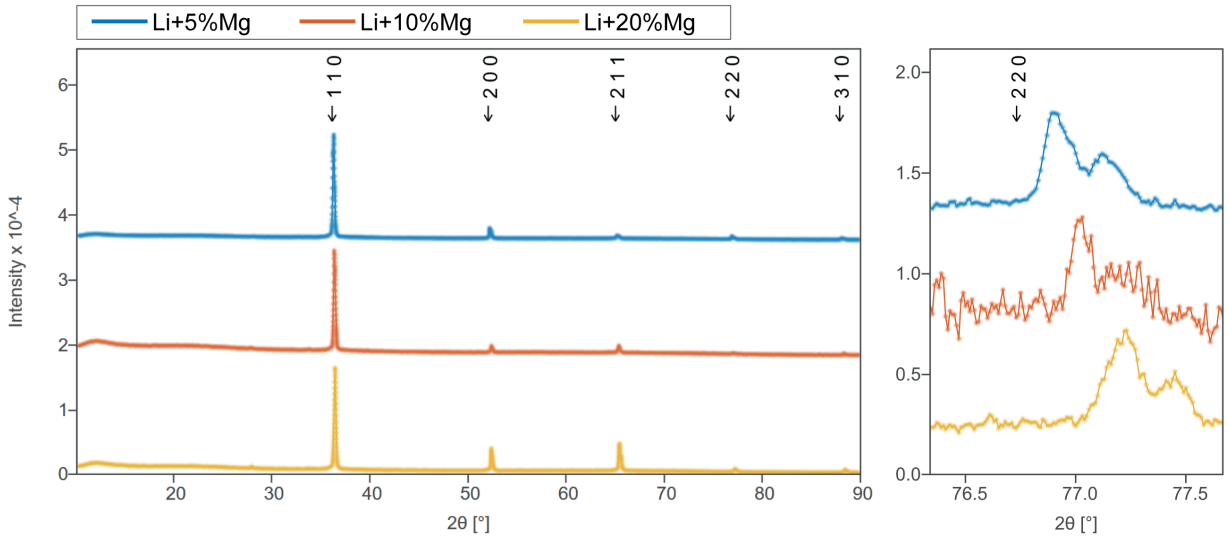

Figure S1. (a) X-ray diffraction of lithium alloys. (b) Zoomed panel showing peak shift with increased magnesium content.

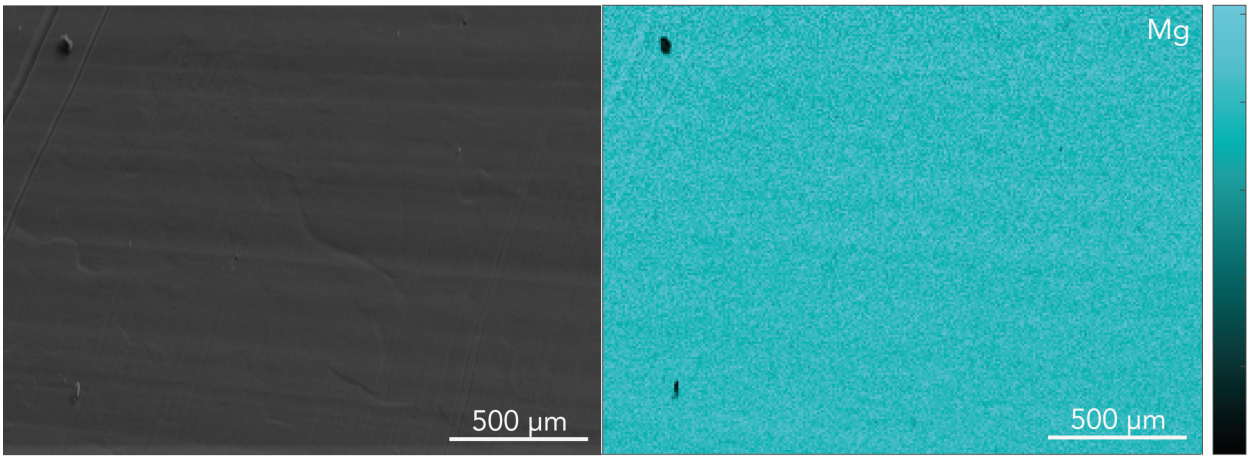

Figure S2. (a) SEM image of Li+5at%Mg sample surface. (b) Corresponding energy dispersive x-ray spectroscopy (EDX) map of Li+5at%Mg sample. Showing homogeneous Mg distribution throughout the sample.

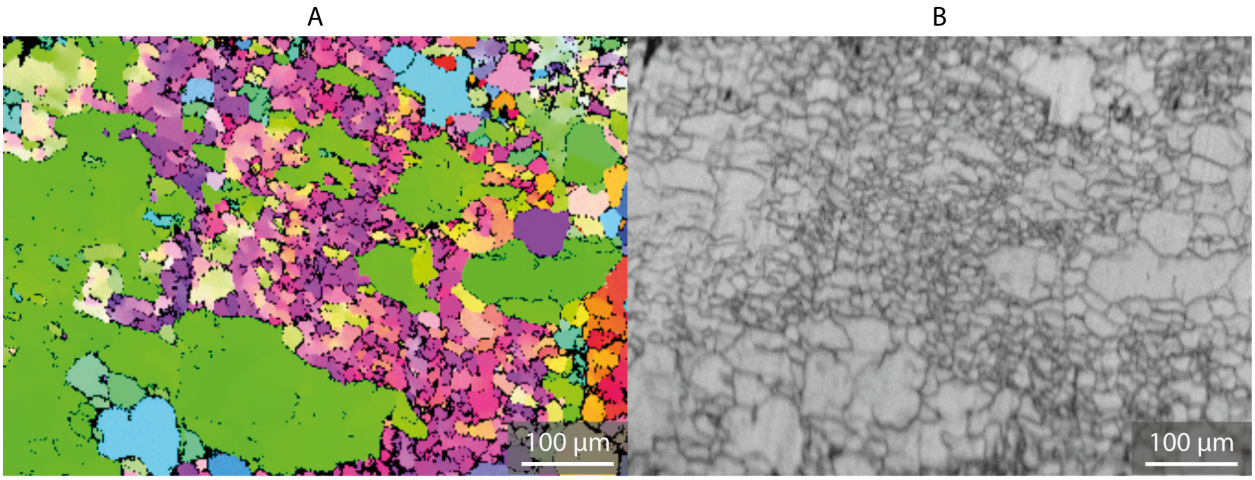

Figure S3. EBSD map of dendritic Li+20at%Mg microstructure. (a) EBSD IPF Z map. Large regions with similar orientation are observed. (b) Band constrast of same region. Shows clear sub-grain boundaries within dendritic regions.

Example of a dendritic solidification microstructure in Li+20at%Mg alloy, slow cooled overnight in a furnace from 450°C. Large regions can be seen in the orientation map, with grain boundaries visible in the band contrast map, and in unresolved orientation points. This microstructure is the result of dendritic solidification due to constitutional supercooling.

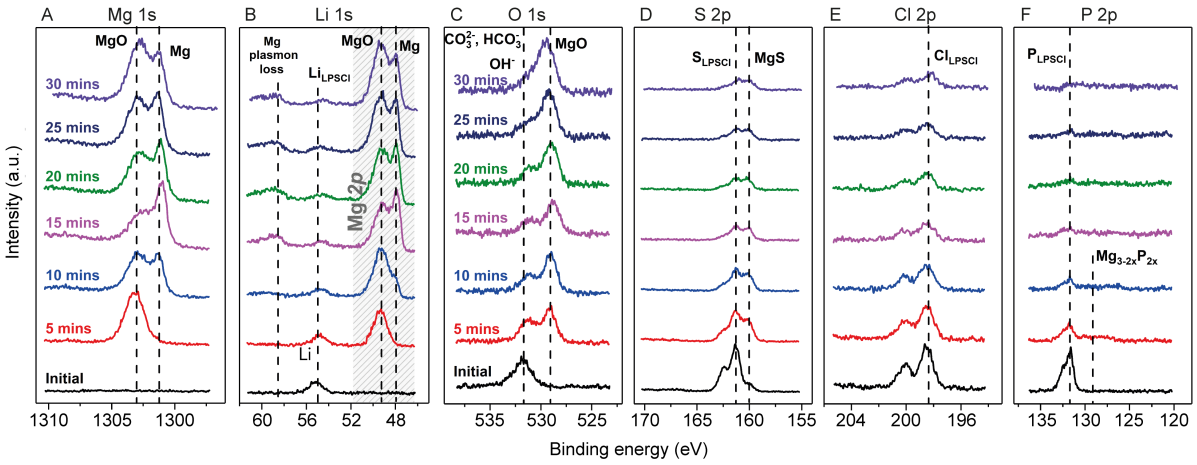

Figure S4. XPS data of Mg sputtered in-situ onto Li6PS5Cl. Core-level XPS spectra collected at 5 min intervals during Mg sputtering conducted over a total period of 30 mins, for (a) Mg 1s, (b) Li 1s, (c) O 1s, (d) S 2p, (e) Cl 2p, and (f) P 2p transitions.

To investigate the possible reaction products formed from the presence of magnesium within the alloy anodes, pure magnesium metal was sputtered in-situ [1] onto an argyrodite pellet using an Ar+ ion gun and the evolving interphase was characterised using x-ray photoemission spectroscopy (XPS). Fig. S4A-B show core-level XPS spectra for the Mg 1s and Li 1s transitions from the surface of the pellet, at various intervals during etching of a magnesium foil. The initial oxygen 1s spectra reveals the presence of surface contamination comprising typically of carbonates, bicarbonates and hydroxides, whose intensity reduces with increased Mg sputtering. After just five minutes of sputtering (at an Ar^+ ion accelerating voltage of 4 kV) a peak characteristic of magnesium oxide appears at a binding energy (B.E.) of 1303 eV in the Mg 1s spectra, with an equivalent peak appearing in the oxygen 1s spectra at a B.E. of 529 eV [2]. Despite the very low oxygen content of the XPS chamber, the metallic magnesium layer deposited can easily react to form MgO [3, 4]. Further magnesium sputtering results in the appearance of another Mg 1s peak at a lower B.E. (∼1301 eV) characteristic of metallic magnesium, that increases in intensity as sputtering proceeds for longer periods. The electrochemical potential of pure magnesium is well below the stability window of Li_6PS_5Cl, so it will be reduced with magnesium deposition. Li_6PS_5Cl reacts with lithium to form Li_2S, suggesting that the S^{2-} is weakly bound within the $PS_4{}^{3-}$ tetrahedron. [5]. The growth of a peak at the lower B.E. shoulder (∼160 eV) in the S 2p spectra (Fig. S4D) could be indicative of the formation of MgS [6] but is indistinguishable from an Li_2S peak. The same is true in the Mg 1s spectra, where any MgS peak would be at a B.E. similar to that of MgO [7, 8], but the growth of this peak after 15 minutes perhaps suggests the formation of MgS. No significant changes in the Cl 2p spectra were observed (Fig. S4E), likely due to the proximity in B.E. values for the Cl in argyrodite and that in $MgCl_2$, as has been noted previously for LiCl [5]. Lastly, in the P 2p spectra (Fig. S4F) there is a broad feature between 126-130 eV, ascribed to the formation of sub-phosphides which has equivalently been observed in the case of lithium sputtering [9], is present in very low intensities between five and ten minutes of sputtering.

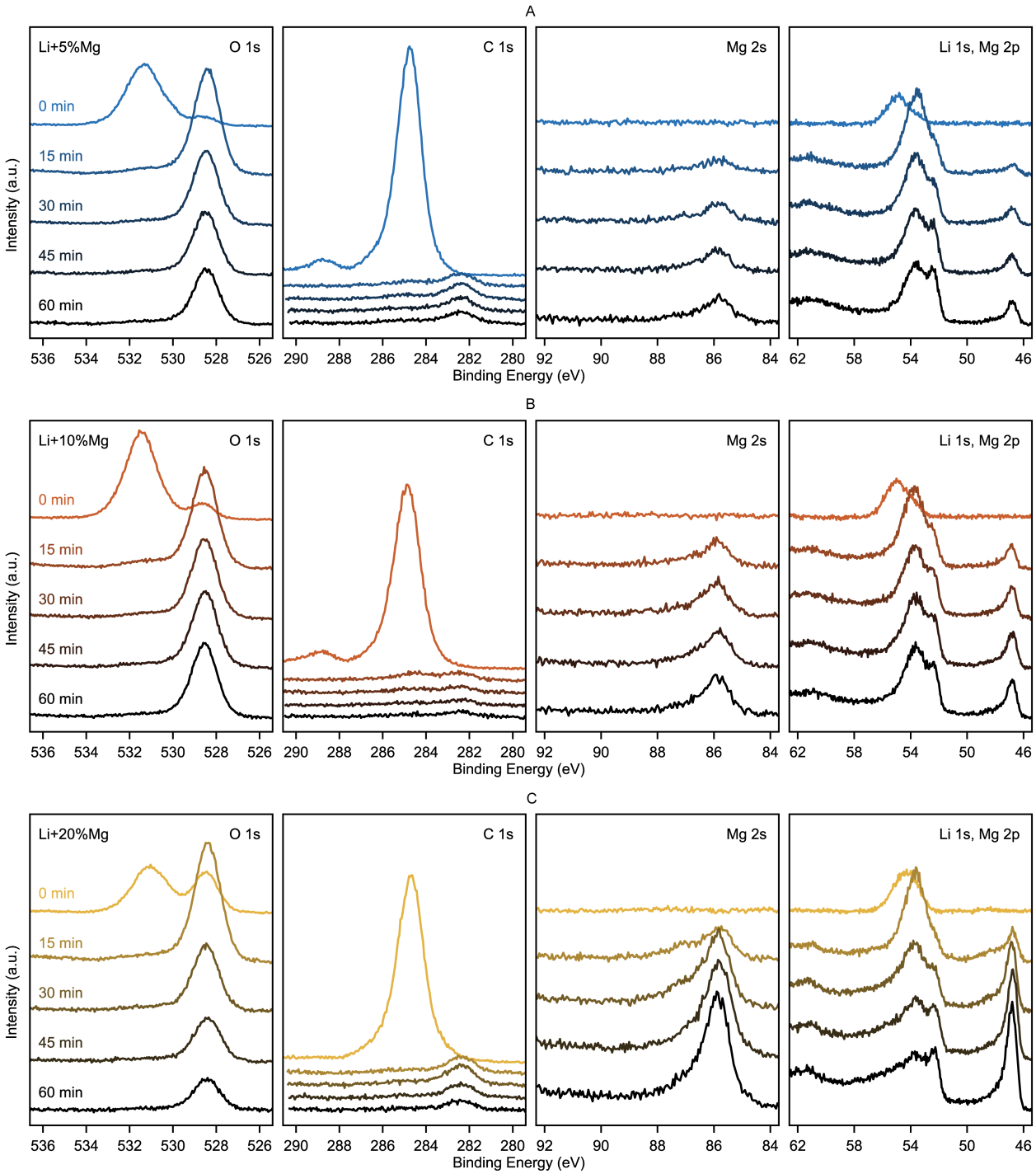

Figure S5. XPS analysis to characterise native layer on alloy surface. Core-level XPS spectra for each alloy composition for O 1s, C 1s, Mg 2s, Li 1s and Mg 2p conducted at 15-minute intervals during argon sputtering conducted over a total period of 60 mins. (a) Li+5%Mg, (b) Li+10%Mg, (c) Li+20%Mg.

5

	^{6}Li diffusion coefficient ($\times 10^{-9}$ cm^{2}s^{-1})			
Temperature (°C)	Lithium	5% Mg	10% Mg	20% Mg
373.1	4.04(57)		1.26(14)	
383.1	5.75(24)	3.36(90)	2.18(19)	
393.1	8.83(37)	4.99(13)	3.00(10)	1.96(19)
403.1	11.9(11)	7.68(16)	4.60(16)	
413.1		11.65(22)		4.57(30)
423.1		18.28(49)		6.41(36)
433.1				10.6(40)

Table S1. Diffusion coefficients measured with 6Li PFG-NMR.

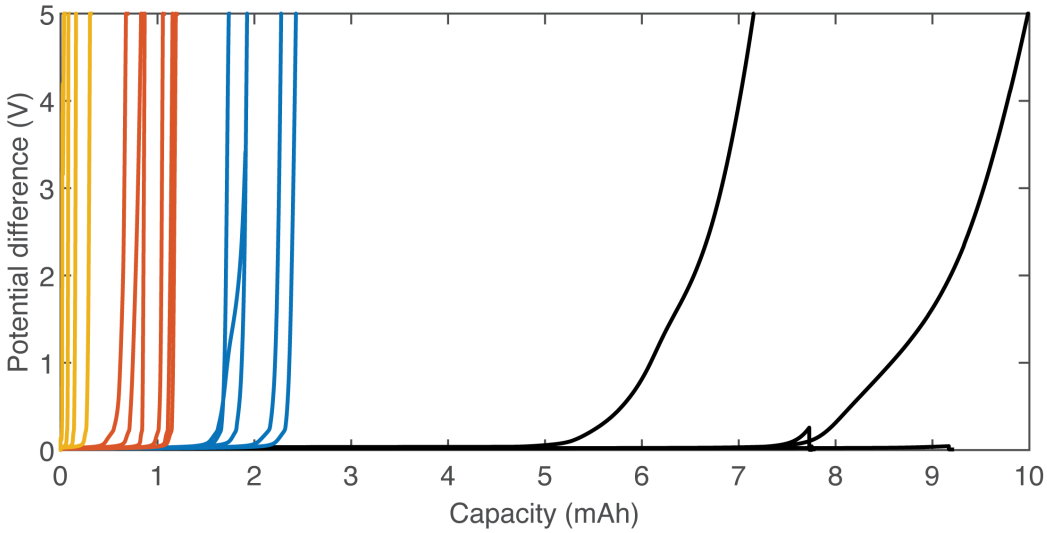

Figure S6. Chronopotentiometry with all curves for tested alloys. Selected representative data reproduced in main text.

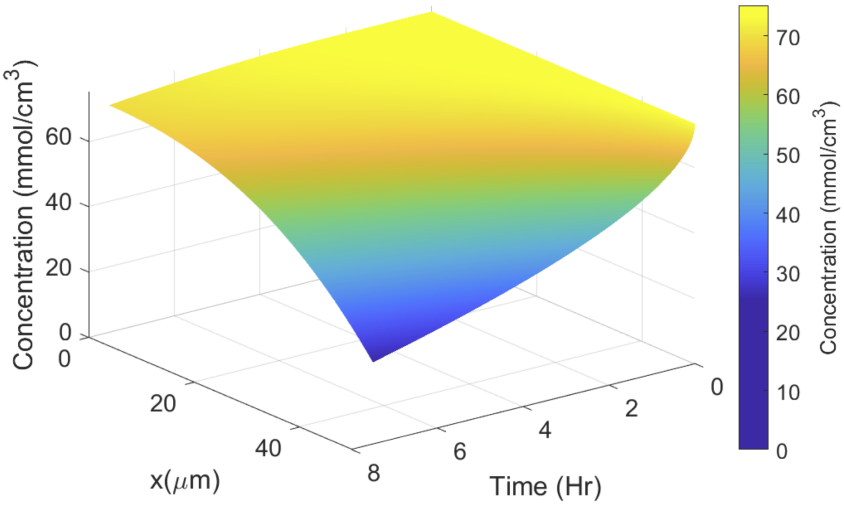

Figure S7. Modelled concentration profile over time in a lithium 5% magnesium alloy anode, with an effective diffusivity of $1.52 \times 10^{-10}\text{cm}^2\text{s}^{-1}$.

Diffusion model

Diffusion within lithium magnesium alloys was modelled using the Crank-Nicolson method as the analytical solution has a boundary condition problem [10]. Fick's second law of diffusion, equation (1), can be discretized at a given point in space and time in either the implicit backward time, central space (BTCS) or the explicit forward time, central space (FTCS).

$$\frac{\partial \mathrm{C}}{\partial \mathrm{t}} = \mathrm{D}\frac{\partial^2 \mathrm{C}}{\partial \mathrm{x}^2} \tag{1}$$

Backward time central space (BTCS):

$$\frac{\mathrm{C}_\mathrm{j}^{\mathrm{n}+1} - \mathrm{C}_\mathrm{j}^{\mathrm{n}}}{\Delta \mathrm{t}} = \mathrm{D}\frac{\frac{\mathrm{C}_{\mathrm{j}+1}^{\mathrm{n}+1} - \mathrm{C}_\mathrm{j}^{\mathrm{n}+1}}{\Delta \mathrm{x}} - \frac{\mathrm{C}_\mathrm{j}^{\mathrm{n}+1} - \mathrm{C}_{\mathrm{j}-1}^{\mathrm{n}+1}}{\Delta \mathrm{x}}}{\Delta \mathrm{x}} \tag{2}$$

$$\frac{\mathrm{C}_\mathrm{j}^{\mathrm{n}+1} - \mathrm{C}_\mathrm{j}^{\mathrm{n}}}{\Delta \mathrm{t}} = \mathrm{D}\frac{\mathrm{C}_{\mathrm{j}+1}^{\mathrm{n}+1} - 2\mathrm{C}_\mathrm{j}^{\mathrm{n}+1} + \mathrm{C}_{\mathrm{j}-1}^{\mathrm{n}+1}}{(\Delta \mathrm{x})^2} \tag{3}$$

Forward time central space (FTCS):

$$\frac{\mathrm{C}_\mathrm{j}^{\mathrm{n}+1} - \mathrm{C}_\mathrm{j}^{\mathrm{n}}}{\Delta \mathrm{t}} = \mathrm{D}\frac{\mathrm{C}_{\mathrm{j}+1}^{\mathrm{n}} - 2\mathrm{C}_\mathrm{j}^{\mathrm{n}} + \mathrm{C}_{\mathrm{j}-1}^{\mathrm{n}}}{(\Delta \mathrm{x})^2} \tag{4}$$

The Crank-Nicolson method averages these two, giving an expression that is stable for a general time interval.

$$\frac{\partial \mathrm{C}}{\partial \mathrm{t}} = \frac{\mathrm{D}}{2}\left\{\frac{\partial^2 \mathrm{C}}{\partial \mathrm{x}^2}_{\,\mathrm{BTCS}} + \frac{\partial^2 \mathrm{C}}{\partial \mathrm{x}^2}_{\,\mathrm{FTCS}}\right\} \tag{5}$$

$$\frac{\mathrm{C}_\mathrm{j}^{\mathrm{n}+1} - \mathrm{C}_\mathrm{j}^{\mathrm{n}}}{\Delta \mathrm{t}} = \frac{\mathrm{D}}{2}\left(\frac{\mathrm{C}_{\mathrm{j}+1}^{\mathrm{n}} - 2\mathrm{C}_\mathrm{j}^{\mathrm{n}} + \mathrm{C}_{\mathrm{j}-1}^{\mathrm{n}}}{(\Delta \mathrm{x})^2} + \frac{\mathrm{C}_{\mathrm{j}+1}^{\mathrm{n}+1} - 2\mathrm{C}_\mathrm{j}^{\mathrm{n}+1} + \mathrm{C}_{\mathrm{j}-1}^{\mathrm{n}+1}}{(\Delta \mathrm{x})^2}\right) \tag{6}$$

Let $\alpha = \frac{\mathrm{D}\Delta \mathrm{t}}{(\Delta \mathrm{x})^2}$, and rearrange to group the **n+1** terms on the right-hand side.

$$-\frac{\alpha}{2}\mathrm{C}_{\mathrm{j}-1}^{\mathrm{n}} + (1+\alpha)\,\mathrm{C}_\mathrm{j}^{\mathrm{n}} - \frac{\alpha}{2}\mathrm{C}_{\mathrm{j}+1}^{\mathrm{n}} = \frac{\alpha}{2}\mathrm{C}_{\mathrm{j}-1}^{\mathrm{n}+1} + (1-\alpha)\,\mathrm{C}_\mathrm{j}^{\mathrm{n}+1} + \frac{\alpha}{2}\mathrm{C}_{\mathrm{j}+1}^{\mathrm{n}+1} \tag{7}$$

This set of simultaneous equations for C_1 to C_N can be written in matrix form. A compressed version of this is of the form:

$$\begin{bmatrix} 1+\alpha & -\frac{\alpha}{2} & 0 & 0 \\ -\frac{\alpha}{2} & 1+\alpha & -\frac{\alpha}{2} & 0 \\ 0 & -\frac{\alpha}{2} & 1+\alpha & -\frac{\alpha}{2} \\ 0 & 0 & -\frac{\alpha}{2} & 1+\alpha \end{bmatrix} \cdot \begin{bmatrix} \mathrm{C}_1^{\mathrm{n}} \\ \vdots \\ \vdots \\ \mathrm{C}_\mathrm{N}^{\mathrm{n}} \end{bmatrix} = \begin{bmatrix} 1-\alpha & \frac{\alpha}{2} & 0 & 0 \\ \frac{\alpha}{2} & 1-\alpha & \frac{\alpha}{2} & 0 \\ 0 & \frac{\alpha}{2} & 1-\alpha & \frac{\alpha}{2} \\ 0 & 0 & \frac{\alpha}{2} & 1-\alpha \end{bmatrix} \cdot \begin{bmatrix} \mathrm{C}_1^{\mathrm{n}+1} \\ \vdots \\ \vdots \\ \mathrm{C}_\mathrm{N}^{\mathrm{n}+1} \end{bmatrix} \tag{8}$$

The corners of this matrix differ due to boundary conditions. For insulative conditions:

$$\mathrm{C}_{\mathrm{j}-1}^{\mathrm{n}} = \mathrm{C}_\mathrm{j}^{\mathrm{n}} \tag{9}$$

$$\left(1+\frac{\alpha}{2}\right)\mathrm{C}_\mathrm{j}^{\mathrm{n}} - \frac{\alpha}{2}\mathrm{C}_{\mathrm{j}+1}^{\mathrm{n}} = \left(1-\frac{\alpha}{2}\right)\mathrm{C}_\mathrm{j}^{\mathrm{n}+1} + \frac{\alpha}{2}\mathrm{C}_{\mathrm{j}+1}^{\mathrm{n}+1} \tag{10}$$

A constant flux condition was achieved computationally by modelling the right-hand boundary as insulative and then subtracting from the boundary concentration each timestep.

$$\begin{bmatrix} 1+\frac{\alpha}{2} & -\frac{\alpha}{2} & 0 & 0 \\ -\frac{\alpha}{2} & 1+\alpha & -\frac{\alpha}{2} & 0 \\ 0 & -\frac{\alpha}{2} & 1+\alpha & -\frac{\alpha}{2} \\ 0 & 0 & -\frac{\alpha}{2} & 1+\frac{\alpha}{2} \end{bmatrix} \cdot \begin{bmatrix} C_1^n \\ \vdots \\ \vdots \\ C_N^n \end{bmatrix} = \begin{bmatrix} 1-\frac{\alpha}{2} & \frac{\alpha}{2} & 0 & 0 \\ \frac{\alpha}{2} & 1-\alpha & \frac{\alpha}{2} & 0 \\ 0 & \frac{\alpha}{2} & 1-\alpha & \frac{\alpha}{2} \\ 0 & 0 & \frac{\alpha}{2} & 1-\frac{\alpha}{2} \end{bmatrix} \cdot \begin{bmatrix} C_1^{n+1} \\ \vdots \\ \vdots \\ C_N^{n+1} \end{bmatrix} \tag{11}$$

This expression can be rewritten as follows, and then C^{n+1} solved by inversion and multiplication. The matrix was stored in the sparse datatype, as most of the values are zero.

$$M_L^n \cdot C^n = M_R^{n+1} \cdot C^{n+1} \tag{12}$$

$$C^{n+1} = \left(M_R^{n+1}\right)^{-1} \cdot M_L^n \cdot C^n \tag{13}$$

This methodology is applicable to multi-dimensional systems and can be adapted to integrate concentration dependent diffusion or spatially varied diffusivity. The concentration was started at 73.28, 69.71 and 62.47 mmolcm^{-3} for the 5, 10 and 20% alloys respectively; and the diffusion limit point was defined as the solubility limit of the beta phase lithium (69%) or 25.20 mmolcm^{-3}. These concentrations were calculated using the lattice parameter trend from [11]. For the lithium case, the limit was defined as when the surface concentration reached zero, from a starting concentration of 76.83 mmol/cm^3, these lithium values match the Cottrell equation. Diffusivity values were iterated such that the predicted time-to-limit matched experimental data, giving effective diffusivity. As noted earlier, this simple diffusion model does not include any modification of the diffusion behavior due to stress [12].

References

1. Narayanan, S. *et al.* Effect of current density on the Li-Li 6 PS 5 Cl solid electrolyte interphase, 1–11 (2022).
2. Otto, S. K. *et al.* In-Depth Characterization of Lithium-Metal Surfaces with XPS and ToF-SIMS: Toward Better Understanding of the Passivation Layer. *Chemistry of Materials* **33,** 859–867 (2021).
3. Wood, K. N. *et al.* Operando X-ray photoelectron spectroscopy of solid electrolyte interphase formation and evolution in Li2S-P2S5 solid-state electrolytes. *Nature Communications* **9,** 1–10 (2018).
4. Gibson, J. S. *et al.* Gently does it!: in situ preparation of alkali metal-solid electrolyte interfaces for photoelectron spectroscopy. *Faraday Discussions* **236,** 267–287 (2022).
5. Wenzel, S., Sedlmaier, S. J., Dietrich, C., Zeier, W. G. & Janek, J. Interfacial reactivity and interphase growth of argyrodite solid electrolytes at lithium metal electrodes. *Solid State Ionics* **318,** 102–112 (2018).
6. Salama, M. *et al.* Metal-Sulfur Batteries: Overview and Research Methods. *ACS Energy Letters* **4,** 436–446 (2019).
7. Lahtinen, J., Vaari, J., Talo, A., Vehanen, A. & Hautojärvi, P. Studies of Mg-O overlayers on Co(0001): growth mode and CO chemisorption properties. *Surface Science* **245,** 244–254 (1991).
8. Vinayan, B. P. *et al.* Performance study of magnesium-sulfur battery using a graphene based sulfur composite cathode electrode and a non-nucleophilic Mg electrolyte. *Nanoscale* **8,** 3296–3306 (2016).
9. Schwietert, T. K. *et al.* Clarifying the relationship between redox activity and electrochemical stability in solid electrolytes. *Nature Materials* **19,** 428–435 (2020).
10. Krauskopf, T., Mogwitz, B., Rosenbach, C., Zeier, W. G. & Janek, J. Diffusion Limitation of Lithium Metal and Li–Mg Alloy Anodes on LLZO Type Solid Electrolytes as a Function of Temperature and Pressure. *Advanced Energy Materials* **9** (2019).
11. Firth, L. D., Nowaira, N. H. A. & Scott, W. Lattice parameters of lithium-magnesium and lithium-silver alloys. *Journal of Physics F: Metal Physics* **4,** 9–11 (1974).
12. Capone, I. *et al.* Electrochemo-Mechanical Properties of Red Phosphorus Anodes in Lithium, Sodium, and Potassium Ion Batteries. *Matter* **3,** 2012–2028 (2020).